

Framework for Multi-messenger Inference from Neutron Stars: Combining Nuclear Theory Priors

Praveer Tiwari,^{1,2,*} Dake Zhou,³ Bhaskar Biswas,^{4,5,6} Michael McNeil Forbes,^{2,7} and Sukanta Bose^{2,4}

¹*Department of Physics, Indian Institute of Technology Bombay, Mumbai, Maharashtra, India 400076*

²*Department of Physics and Astronomy, Washington State University, Pullman, WA, USA 99164*

³*Department of Physics, University of California, Berkeley, CA, USA 94720[†]*

⁴*Inter-University Centre for Astronomy and Astrophysics, Post Bag 4, Ganeshkhind, Pune 411 007, India*

⁵*The Oskar Klein Centre, Department of Astronomy,
Stockholm University, AlbaNova, SE-10691 Stockholm, Sweden*

⁶*Universität Hamburg, D-22761 Hamburg, Germany[‡]*

⁷*Department of Physics, University of Washington, Seattle, WA, USA 98105[§]*

(Dated: 2024-06-26)

We construct an efficient parameterization of the pure neutron-matter equation of state (EOS) that incorporates the uncertainties from both chiral effective field theory (χ EFT) and phenomenological potential calculations. This parameterization yields a family of EOSs including and extending the forms based purely on these two calculations. In combination with an agnostic inner core EOS, this parameterization is used in a Bayesian inference pipeline to obtain constraints on the EOS parameters using multi-messenger observations of neutron stars. We specifically considered observations of the massive pulsar J0740+6620, the binary neutron star coalescence GW170817, and the calculations on the NICER data from pulsar PSR J0030+0451 and PSR J0740+6620. Constraints on neutron star mass-radius relations are obtained and compared. The Bayes factors for the different EOS models are also computed. While current constraints do not reveal any significant preference among these models, the framework developed here may enable future observations with more sensitive detectors to discriminate them.

I. Introduction

Astrophysical observations of gravitational waves from the binary neutron star merger GW170817 [1, 2] by the LIGO-Virgo collaboration [3, 4], its electromagnetic counterparts [5, 6], and millisecond-pulsar X-rays by NICER [7–10], provide multi-messenger information about the structure of neutron stars. These observations, combined with advances in nuclear theory, give a fillip to the quest of characterizing neutron-rich matter. This quest requires a framework to calculate observables like the neutron star mass M , radius R , and tidal deformability Λ , from a nuclear equation of state (EOS) that can incorporate priors from different forms of nuclear theory. Here we consider priors from quantum Monte Carlo (QMC) with phenomenological potentials, and chiral effective field theory χ EFT.

Experiments and nuclear theory efforts have constrained the nuclear EOS at lower densities, but leave considerable uncertainties above the nuclear saturation density $n_0 \approx 0.16 \text{ fm}^{-3}$. Phenomenological models based on two- and three-body nucleon forces [11–14] have traditionally been used to extrapolate to high density ($\sim 5n_0$ [14]) with somewhat *ad hoc* uncertainty quantification. More recently, χ EFT has demonstrated rather accurate predictions with quantified uncertainties for low-density EOS [15], but questions of convergence cause these uncertainties to grow rapidly at higher densities: These are currently worse than 25% above $2n_0$ [16–18]. This has led to a proliferation of neutron star EOS models used in the astrophysics community [19], many of which are poorly linked to

the underlying physics.

Recent works assume either specific nuclear models or agnostic functionals to constrain the EOS of neutron stars with astrophysical observations. (See e.g. [19–32].) These typically depend on a dominant parabolic expansion centered around symmetric nuclear matter to constrain the neutron-matter EOS. Here, we instead extend the Forbes-Reddy-Zhou (FRZ) EOS model of [33] that constructs a physically motivated EOS by expanding about pure neutron matter, incorporating the properties of symmetric nuclear matter as constraints on this expansion. This provides an alternative perspective that focuses on neutron-rich matter, including only the minimal dependence required to be consistent with symmetric nuclear matter. Our extension adds sufficient flexibility to incorporate both χ EFT [15] results (which we hereafter refer to as χ EFT data) and phenomenological potential-based QMC calculations (which we hereafter refer to as ϕ QMC data using ϕ as a mnemonic for phenomenological) [34–36]). Our model smoothly interpolates between these data with a parameter $\zeta \in [0, 1]$. This allows us to directly infer the underlying nuclear EOS in the Bayesian framework with physically motivated priors. We additionally extend the FRZ EOS with a more generalized EOS for the inner core $n > n_c$ consisting of 3 piecewise polytropes that we smoothly attach at a transition density chosen from $n_c \in \{1.5n_0, 2.0n_0\}$.

Nomenclature — We refer to the last EOS described above as $\text{FRZ}_{n_c/n_0}^\zeta$, where $\zeta = 0$ directly models the χ EFT data [15], $\zeta = 1$ directly models the ϕ QMC data [34–36], and $n_c/n_0 \in \{1.5, 2.0\}$ describes the density n_c where the transition to the polytropic inner-core occurs. Thus, we refer to models like $\text{FRZ}_{1.5}^\chi \equiv \text{FRZ}_{1.5}^{\zeta=0}$ to denote those that are fit to the χ EFT data with a core-transition at $n_c = 1.5n_0$, and $\text{FRZ}_{2.0}^\phi \equiv \text{FRZ}_{2.0}^{\zeta=1}$ for models fit to the ϕ QMC data with a core transition at $n_c = 2.0n_0$, etc. We refer to models where we let ζ vary as “hybrid” models.

* praveer.tiwari@iitb.ac.in

[†] dkzhou@berkeley.edu

[‡] phybhaskar95@gmail.com

[§] m.forbes@wsu.edu

II. Equation of state

The composition of a neutron star varies as the pressure increases with depth. In the outer crust, the mass and neutron number of nuclei increase with pressure. Crossing to the inner crust at the drip line [37], neutrons drip out of the nuclei and accumulate in the interstitial space [38], forming a neutron superfluid that is well modeled as a unitary Fermi gas (UFG) [39]. Deeper nuclei deform, forming regions of nuclear “pasta” [40] that eventually merge into a homogeneous phase of protons, neutrons, and electrons at the start of the outer core. In the inner core when $n \gtrsim 2n_0$, the physics becomes uncertain: Plausible speculations include transitions to hyperonic matter, strange quark matter, and color superconducting matter [41–44].

To describe the interior of neutron stars, efforts have been made to build unified effective EOS [33, 45, 46] that self-consistently bridge the tabulated properties of the outer crust [47] with the homogeneous outer core by using a compressible liquid drop model (CLDM). The CLDM models the transition from nuclei to homogeneous matter with a spherical Wigner-Seitz cell containing the nuclei, the interstitial neutron superfluid, and the lepton gas. While this precludes a formal analysis of more complicated pasta phases and related dynamical phenomena like shear modes associated with these rigid structures, it provides a quantitatively accurate characterization of the EOS because the energy difference between competing pasta phases is small [40, 48].

As mentioned above, a unique property of the unified FRZ EOS [33] that we extend here is the expansion about pure neutron matter. As shown in [33] and confirmed by our global sensitivity analysis in Appendix 4, this approach is quite insensitive to the properties of symmetric nuclear matter, allowing astrophysical observables to directly constrain the properties of neutron-rich matter. While consistent with global fits to nuclear data [49], this insensitivity differs markedly from analyses that assume a dominant quadratic iso-spin expansion. One appeal of a dominant quadratic expansion is that one can directly relate the full symmetry energy S and its slope L with the corresponding coefficients S_2 and L_2 in the quadratic expansion about the symmetric nuclear matter that is constrained with terrestrial experiments.

While this quadratic dominance has some support at low densities [50] and appears to hold in effective field theory (EFT)-based calculations [15], recent tension arising from neutron skin measurements [51] highlight the subtleties and challenges in faithfully extracting S and L . Our approach is complementary, directly connecting observations with the full parameters S and L , but breaking the connection with S_2 and L_2 . Further explicit assumptions about the iso-spin expansion must be added to our model if any significant connection between observations and S_2 and L_2 are desired [33].

We extend the FRZ EOS in two ways. First, we find a new parameterization of the pure neutron-matter EOS that consistently incorporates both the original double polytropic parameterization of [36], and state-of-the-art EFT calculation at N3LO [15] with a single new parameter ζ that smoothly interpolates from one dataset to the other. Second, we update the inner core model, replacing the quadratic speed-of-sound EOS that was

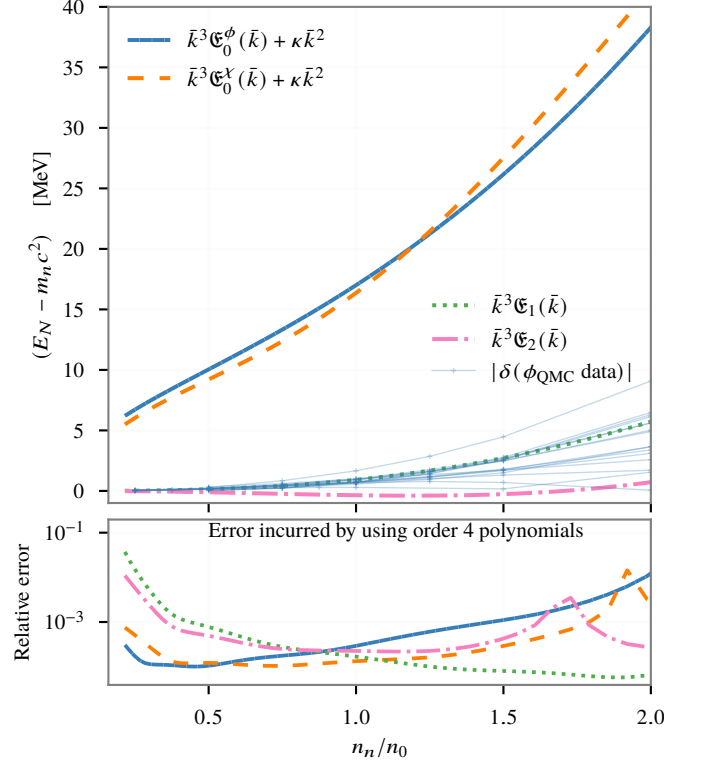


Figure 1. The fourth-order polynomial $\mathfrak{E}(\bar{k})$, which defines the energy per neutron in Eq. (1), is expanded in the basis of $\mathfrak{E}_{1,2}$ (see Eq. (2)) about the mean \mathfrak{E}_0 . The basis functions $\mathfrak{E}_{1,2}$ are fourth-order polynomials in \bar{k} (plotted with dotted and dash-dot lines) obtained by fitting the two most significant vectors of the covariance matrix of $(E_N(\bar{k}) - m_n c^2 - \kappa \bar{k}^2)/\bar{k}^3$ coming from χ EFT data. The means for the χ EFT and ϕ QMC data are fitted with fourth-order polynomials (in \bar{k}) to obtain \mathfrak{E}_0^χ (dashed line) and \mathfrak{E}_0^ϕ (solid line). Also plotted (thin solid lines near the dotted line) are the deviations from \mathfrak{E}_0^ϕ for different realizations of ϕ QMC EOSs.

artificially constrained by a conjectured analogy with finite temperature QCD, with a piecewise polytrope parameterization [19, 26] that allows for greater variations in this poorly understood region.

A. Pure Neutron Matter

We characterize the EOS of pure neutron matter in terms of the energy per particle $E_N = \mathcal{E}(n_n)/n_n$, where \mathcal{E} is the energy density and n_n the neutron number density. While the energy calculated (ϕ QMC [36, 52]) from the phenomenological potentials [34–36] can be modeled well by the double polytrope $E_N \propto a n_n^\alpha + b n_n^\beta$ used in [33], this form is not sufficiently flexible to accurately model the χ EFT data [15]. We found a polynomial fit to the energy per neutron that captures both the central values and correlated uncertainties of both models.

We model the energy per neutron as

$$E_N(\bar{k}) = m_n c^2 + \kappa \bar{k}^2 + \bar{k}^3 \mathfrak{E}(\bar{k}), \quad (1)$$

where $\mathfrak{E}(\bar{k})$ is a fourth-order polynomial of the dimensionless parameter $\bar{k} \equiv (n_n/n_0)^{1/3}$, which is proportional to the Fermi momentum. The first $\kappa \bar{k}^2$ term ensures that Eq. (1) approaches the EOS of the UFG at low densities. This is consistent with the analysis in [49] that we use to fix the value of $\kappa = 25.5$ MeV.

For the χ EFT data, Drischler *et al.* [15] characterize the truncation errors with a Gaussian process [53]. This gives a covariance matrix with two dominant principle components that account for more than 95% of the uncertainties, which is sufficient for current astrophysical analyses. To this level, we can thus faithfully characterize this χ EFT dataset with three fixed polynomials (see Fig. 1):

$$\mathfrak{E}^X(\bar{k}) = \mathfrak{E}_0^X(\bar{k}) + a_1 \mathfrak{E}_1(\bar{k}) + a_2 \mathfrak{E}_2(\bar{k}), \quad (2)$$

where $\mathfrak{E}_0^X(\bar{k})$ fits the central values, and $\mathfrak{E}_{1,2}(\bar{k})$ fit the two dominant principal components of the covariance matrix. We find that fourth-order polynomials are sufficient, and scale $\mathfrak{E}_{1,2}(\bar{k})$ appropriately so that $a_{1,2} \in [-2, 2]$ captures the 2σ uncertainty region.

For the ϕ QMC data, Gandolfi *et al.* [34, 35, 36] performed multiple QMC calculations for a variety of phenomenological potentials that include both two- and three-body contributions. As we discuss in Appendix 2, all of these data can also be efficiently described by three analogous fourth-order polynomials: $\mathfrak{E}_0^\phi(\bar{k})$ fitting the central values, and $\mathfrak{E}_{1,2}^\phi(\bar{k})$ fitting the correlated variations in the data.

Surprisingly, although the central values $\mathfrak{E}_0^\phi(\bar{k})$ differ from $\mathfrak{E}_0^X(\bar{k})$, it turns out that the spread in the ϕ QMC data is well described by the *same* uncertainty model $a_{1,2} \in [-2, +2]$ with the same $\mathfrak{E}_{1,2}(\bar{k})$ as the χ EFT data, (though not with the same rigorous meaning of 2σ). Perhaps this surprising relationship hints at a consistency between the two physically-inspired microscopic approaches, or provides insight into the physics of many-nucleon systems.

In any case, we can thus accurately parameterize both sets of data with a three-parameter model (ζ, a_1, a_2):

$$\mathfrak{E}(\bar{k}) = \left(\zeta \mathfrak{E}_0^\phi(\bar{k}) + (1 - \zeta) \mathfrak{E}_0^X(\bar{k}) \right) + a_1 \mathfrak{E}_1(\bar{k}) + a_2 \mathfrak{E}_2(\bar{k}) \quad (3)$$

where the parameter $\zeta \in [0, 1]$ smoothly interpolates between ϕ QMC ($\zeta = 0$) and χ EFT ($\zeta = 1$). The fourth-order polynomials $\mathfrak{E}_0^\phi(\bar{k})$, $\mathfrak{E}_0^X(\bar{k})$, $\mathfrak{E}_1(\bar{k})$, and $\mathfrak{E}_2(\bar{k})$ and the fitting process are described in Appendices 1 and 2.

B. Inner Core

At baryon number densities $n > n_c$ we use a set of three piecewise polytropes $P_i(n)$ [26, 54] to describe homogeneous

matter in beta-equilibrium:

$$P(n) = \begin{cases} P_1(n) & n_1 \equiv n_c < n \leq n_2, \\ P_2(n) & n_2 < n \leq n_3, \\ P_3(n) & n_3 < n, \end{cases} \quad (4a)$$

$$P_i(n) = K_i n^{\Gamma_i}, \quad K_i = \frac{P(n_i)}{n_i^{\Gamma_i}}. \quad (4b)$$

This introduces six new parameters: $\{n_c, n_2, n_3, \Gamma_1, \Gamma_2, \Gamma_3\}$, with the coefficients K_i fixed by demanding that $P(n)$ be continuous. For our analysis, we use the uniform priors listed in Table I for these. The polytropic indices Γ_i control the stiffness of the EOS. $\Gamma_i = 0$ corresponds to a first-order phase transition of size $\Delta n = n_{i+1} - n_i$. As larger polytropic indices could potentially violate causality, we switch to the causal EOS [55] whenever causality is violated.

Table I. Priors for the core EOS parameters (following Ref. [56]), pure-neutron-matter parameters, and u_p . Note that the constraint $n_c \equiv n_1 < n_2$ means that the range of n_2 depends on the value of n_c : i.e., the range of n_2 differs for models FRZ_{1.5} and FRZ_{2.0}. Most priors are uniform, but a_1 and a_2 follow normal distributions truncated at $\pm 2\sigma$. The parameter ζ (last row) is only relevant for the interpolated model FRZ $^\zeta$.

Parameter	Range	Distribution
Γ_1	[1, 4.5]	Uniform
Γ_2	[0, 8]	Uniform
Γ_3	[0.5, 8]	Uniform
n_2	$[n_c, 8.3n_0]$	Uniform
n_3	$[n_2, 8.3n_0]$	Uniform
a_1, a_2	[-2, 2]	Normal(0,1)
u_p	[2.5, 3.7]	Uniform
ζ	[0, 1]	Uniform

C. Parameter Space

As described at the end of the introduction, we explore models

$$\text{FRZ}_{n_c/n_0}^\zeta$$

where ζ interpolates between $\text{FRZ}^{\zeta=0} \equiv \text{FRZ}^\phi$ and $\text{FRZ}^{\zeta=1} \equiv \text{FRZ}^\chi$. For each model, we consider core-transition densities $n_c = 1.5n_0$ and $n_c = 2.0n_0$ as fiducial values to explore the extent to which astrophysical observables rely on low-density nuclear inputs and vice versa. Strong astrophysical signals may inform where low-energy nuclear models break down.

Our models are defined by more than 15 parameters (see Table I in [33] and Table II in [26]). As sampling in such a large space is computationally prohibitive, we limit the number of parameters by performing a global sensitivity analysis based on Sobol indices [57] as detailed in Appendix 4. Fortunately, more than half of the parameters do not significantly influence the astrophysical observables. This is consistent with the local sensitive analysis of [33], but accounts for potential correlations among parameters.

We thus only sample the most significant parameters (beyond n_c) listed in Table I along with their priors. These include the 5 remaining inner core parameters, the two parameters $a_{1,2}$ describing the variations in pure neutron matter, and u_p – a parameter characterizing the self-energy of proton polarons (for detail see [33]). We fix the remaining insignificant parameters – such as those related to the symmetric nuclear matter – at the physically motivated fiducial values described in [33].

III. Bayesian Inference from Astrophysical Observations

To determine how well the available astrophysical data constrain our model, we use Bayesian inference to successively update the priors listed in Table I with the maximum mass constraint from the pulsar (PSR) J0740+6620 [58], tidal deformability constraints from GW170817 [59], radius measurements of PSR J0030+0451 from NICER by Miller *et al.* [8] & Riley *et al.* [7]; and radius measurements of PSR J0740+6620 from NICER & X-ray Multi-Mirror (XMM)-Newton spectroscopy, by the same two groups [9, 10].

Let $\Upsilon = (a_j, n_i, \Gamma_i, \dots)$ be the set of EOS parameters listed in Table I, and d the set of astrophysical data. We express our prior knowledge of the parameters in terms of a probability density function (PDF) $p(\Upsilon)$. Bayes' theorem tells us how to use data d to update our knowledge of the EOS from the probability $p(d|\Upsilon)$ of obtaining the data d given the parameters Υ :

$$p(\Upsilon|d) = \frac{\overbrace{p(d|\Upsilon)p(\Upsilon)}^{\mathcal{L}_d(\Upsilon)}}{Z}, \quad Z = \int d\Upsilon \overbrace{p(d|\Upsilon)p(\Upsilon)}^{\mathcal{L}_d(\Upsilon)}. \quad (5)$$

We refer to the updated knowledge $p(\Upsilon|d)$ as the posterior and Z as the evidence. It is common to call $p(d|\Upsilon) = \mathcal{L}_d(\Upsilon)$ a likelihood but note that the latter is not a PDF for Υ .

As Z simply follows from normalizing the posterior, it is often left implicit, but it provides information about how well the data d supports competing hypotheses (i.e., different models). Ideally, the hypotheses correspond to disjoint regions H_1 and H_2 of parameter space, with $H_1 \cup H_2 = \emptyset$: i.e., model 1 corresponds to $\Upsilon \in H_1$ while model 2 corresponds to $\Upsilon \in H_2$. This is the case, e.g., with FRZ^χ and FRZ^ϕ , which are disjoint because of $\zeta \in \{0, 1\}$. The degree to which the data d favors one hypothesis over the other can be expressed in terms of the ratio \mathcal{B}_{12} called the Bayes factor, where

$$\mathcal{B}_{12} = \frac{Z_{H_1}}{Z_{H_2}} \quad Z_{H_{1,2}} = \int_{\Upsilon \in H_{1,2}} d\Upsilon p(d|\Upsilon) p(\Upsilon). \quad (6)$$

If the Bayes factor is high ($\mathcal{B}_{12} \gtrsim 3.2$), then we say that the dataset d favors hypothesis H_1 over H_2 , and *vice versa* for $\mathcal{B}_{21} \equiv 1/\mathcal{B}_{12} \gtrsim 3.2$. For Bayes factors close to unity one concludes that the data d does not strongly favor one hypothesis over the other [60].

A. Heavy Pulsar PSR J0740+6620

PSR J0740+6620 is one of the heaviest known pulsars and therefore places a constraint on the maximum mass $M_{\text{max}}(\Upsilon)$ of neutron stars supported by the EOS characterized by Υ . Therefore, allowed EOSs must support neutron star masses, M , that are at least as heavy as M_{max} . To impose this maximum-mass constraint on Υ we first construct the PDF of neutron star masses, $p(M, \Upsilon|\text{Pulsar})$, by multiplying the posterior PDF of PSR J0740+6620, $\sim \mathcal{N}(2.08M_\odot, 0.07M_\odot)$ Fonseca *et al.* [58], with the Heaviside step function $H(M_{\text{max}}(\Upsilon) - M)$. The likelihood function for the massive pulsar in Eq. (5) is then computed as

$$\mathcal{L}_{\text{Pulsar}}(\Upsilon) = \int dM p(M, \Upsilon|\text{Pulsar}) p(M), \quad (7)$$

where $p(M)$ is the prior on neutron star masses, which we take to be uniform on $[1, 3]M_\odot$.

B. Tidal deformability from GW170817

Analyses of the gravitational-wave signal from GW170817 [59] provided information on the tidal deformabilities $\Lambda_{1,2}$ of the two neutron stars (with primary and secondary masses m_1 and m_2 , respectively) involved in that binary merger. The posteriors of these observables depend on the prior used for the magnitude of the spins of the neutron stars. Based on the current catalog of observed pulsars, we understand that the magnitude of the spin of neutron stars needs to be less than 0.05 if they are to merge in a Hubble time [59]. Additionally, it can be assumed that both the components of GW170817 have a common EOS, which constrains the two Λ s. The posteriors on the masses and tidal deformabilities are then obtained through Bayesian inference assuming a specific waveform model (such as PhenomPNRT, TaylorF2, etc.) [59].

While the imprint of the EOS in the GW signal of a binary neutron star is mainly sensitive to $\tilde{\Lambda}$, which is a particular combination of $\Lambda_{1,2}$ ¹, one can use the so-called EOS insensitive relations [61, 62] to disentangle the degeneracy in the influence of $\Lambda_{1,2}$ on $\tilde{\Lambda}$ and obtain a joint probability distribution for $(m_1, m_2, \Lambda_1, \Lambda_2)$ from the GW170817 data. Alternatively, this distribution can be computed in terms of $(q, \mathcal{M}, \Lambda_1, \Lambda_2)$, where $q = m_2/m_1$ is the mass ratio and $\mathcal{M} = (m_1 m_2)^{3/5}/(m_1 + m_2)^{1/5}$ is the chirp mass. In principle, employing the EOS insensitive relations introduces a complex dependency on the EOS parameters Υ but, as their name implies, these relations depend only weakly on the EOS. For the mass range implied by GW170817, one can marginalize over EOS models, thereby introducing only a small fractional error of less than 6.5% each for Λ_1 and Λ_2 [61] (see [59] for details). The posterior $p(q, \mathcal{M}, \Lambda_1, \Lambda_2|\text{GW})$ was obtained in this way [63] by using the PhenomPNRT [59] waveform, assuming a common EOS

¹ This combination is just $\tilde{\Lambda} = \frac{16}{13} \frac{(m_1 + 12m_2)m_1^4\Lambda_1 + (m_2 + 12m_1)m_2^4\Lambda_2}{(m_1 + m_2)^5}$

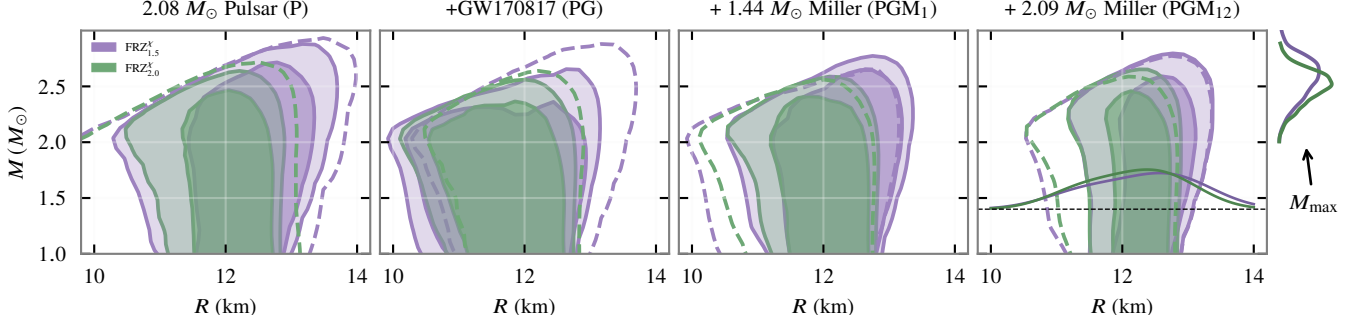


Figure 2. Evolution of the mass-radius posteriors for models $\text{FRZ}_{1.5}^X$ and $\text{FRZ}_{2.0}^X$ as one successively adds, from left to right, mass measurements of the $2.08M_\odot$ pulsar PSR J0030+0451 [58], GW170817, and the results in Miller *et al.* [8, 10] based on the 2019 (PGM₁) and 2021 NICER (PGM₁₂) papers. In the left panel, the dashed lines correspond to 2σ (95%) priors and the nested solid lines / shaded regions correspond to the 1σ (68%) and 2σ posteriors after including the $2.08M_\odot$ mass measurement. These posteriors become the dashed priors in the subsequent panels, and the shaded regions contain the updated 1σ and 2σ posteriors after including the subsequent observations. The posteriors in the right two panels correspond to posteriors PGM₁ and PGM₁₂ respectively in later plots. The rightmost panel shows posterior distributions for $R_{1.4M_\odot}$ and M_{max} .

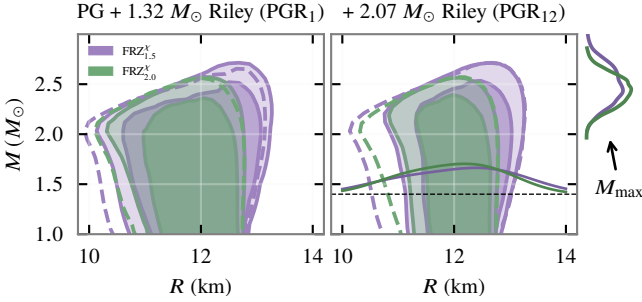


Figure 3. Same as the right two panels of Fig. 2, but replacing the calculations of Miller *et al.* [8, 10] with those of Riley *et al.* [7, 9].

and without the maximum-mass constraint. We next use this posterior to constrain Υ .

Since the chirp mass is well determined to be $M_0 = 1.186(1)M_\odot$ [1], we can essentially fix it and only need to marginalize over the poorly-constrained mass ratio $q = m_2/m_1$ to obtain the GW likelihood:

$$\begin{aligned} \mathcal{L}_{\text{GW}}(\Upsilon) &= \int dq dM p(q, M) \times \\ &\quad p(q, M, \Lambda_1(\Upsilon, q, M), \Lambda_2(\Upsilon, q, M)|_{\text{GW}}) \\ &\approx \int dq p(q) p(q, M_0, \Lambda_1(\Upsilon, q, M_0), \Lambda_2(\Upsilon, q, M_0)|_{\text{GW}}) \end{aligned} \quad (8)$$

where $p(q)$ is a prior that we take to be uniform on $[0.5, 1.0]$.

C. NICER measurements

Finally, we consider calculations based on NICER measurements of PSR J0030+0451 [7, 8] in 2019, and both NICER and XMM-Newton data for PSR J0740+6620 [9, 10] in 2021. The inferred mass-radius with 68% credible intervals (CIs) [64] are, respectively, $(1.44^{+0.15}_{-0.14}M_\odot, 13.02^{+1.24}_{-1.06} \text{ km})$ [8] and $(1.32^{+0.20}_{-0.18}M_\odot,$

$12.77^{+1.35}_{-1.45} \text{ km})$ [7] for PSR J0030+0451; and $(2.09^{+0.09}_{-0.09}M_\odot, 13.59^{+2.33}_{-1.38} \text{ km})$ [10] and $(2.07^{+0.07}_{-0.07}M_\odot, 12.39^{+1.29}_{-0.98} \text{ km})$ [9] for PSR J0740+6620. These give two posteriors of the form $p(M, R|\text{NICER})$ that we use for computing the likelihood

$$\mathcal{L}_{\text{NICER}}(\Upsilon) = \int dM p(M) p(M, R(\Upsilon, M)|_{\text{NICER}}), \quad (9)$$

where $p(M)$ is the mass prior and is taken to be uniform on $[1, 2]M_\odot$ for PSR J0030+0451, and uniform on $[1.5, 2.5]M_\odot$ [21] for PSR J0740+6620. The analysis is insensitive to switching to wider priors.

We combine constraints from the maximum mass discussed in section III A, GW170817 discussed in section III B, and X-ray observations in section III C to obtain multimessenger posteriors on the EOS, from which we compute the posteriors on the mass-radius relation shown in Fig. 2. When using the first NICER measurement reported in Miller *et al.* [8] we label our posterior as PGM₁. Further inclusion of the second measurement Miller *et al.* [10] leads to posteriors labeled PGM₁₂. Following a similar prescription, the mass-radius constraints reported in Riley *et al.* [7] and Riley *et al.* [9] are successively included in a separate analysis to obtain multimessenger posteriors labeled PGR₁ and PGR₁₂ shown in Fig. 3. See [65–68] for details about NICER posteriors $p(M, R(\Upsilon, M)|_{\text{NICER}})$.

The Bayesian sampling in this work is performed using the PyMultiNest package [69], a Python implementation of the MultiNest sampling method [70]. When the astrophysical observations $p(d|\psi)$ are given as discrete samples over the space of astrophysical source parameters ψ , we use kernel-density estimates (KDEs) to compute the data posterior for constructing likelihoods. The bandwidth for the KDE is chosen using Scott’s rule [71].

Table II. Inferred Radius of a $1.4M_\odot$ Neutron Star: 95% CI on the radius (in km) of a $1.4M_\odot$ neutron star for $\text{FRZ}_{1.5}^\chi$ and $\text{FRZ}_{2.0}^\chi$ as one progressively includes astrophysical observations. Under each range is a visual indication of the CI (black) in the band [7, 13.1] (light gray) to facilitate comparison. The tighter constraints using the analysis of Miller *et al.* [8, 10] are highlighted in gray: $R_{1.4} = 12.46^{+0.48}_{-1.02}$ km for $n_c = 1.5 n_0$ and $12.28^{+0.50}_{-0.86}$ km for $n_c = 2.0 n_0$ and shown in Fig. 4.

Source	$R_{1.4M_\odot}$ for $\text{FRZ}_{n_c}^\chi$ (95% CI [km])	
	$n_c = 1.5 n_0$	$n_c = 2.0 n_0$
Prior	[7.85, 13.05]	[8.43, 12.79]
+ $2.08M_\odot$ (J0030+0451)	[10.80, 13.02]	[10.81, 12.73]
+ GW170817 (= PG)	[10.27, 12.82]	[10.50, 12.65]
Miller <i>et al.</i>		
PG + $1.44M_\odot$ (J0740+6620)	[10.89, 12.94]	[10.91, 12.72]
+ $2.09M_\odot$ (J0030+0451)	[11.44, 12.95]	[11.42, 12.78]
Riley <i>et al.</i>		
PG + $1.32M_\odot$ (J0740+6620)	[10.55, 12.88]	[10.74, 12.69]
+ $2.07M_\odot$ (J0030+0451)	[11.05, 12.90]	[11.13, 12.72]

IV. Results and Discussion

Fig. 2 and Fig. 3 show 1σ and 2σ multimessenger posteriors in the mass-radius plane. As has been previously observed in the literature, it is evident that GW170817 favors softer EOS [1] while pulsar mass and radius measurements exclude the very soft EOSs [7–10]. This apparent tension manifests as alternating shifts in the posteriors as the set of observations are sequentially included from left to right in Fig. 2.

We have separately investigated the NICER analyses by Miller *et al.* [8, 10] and Riley *et al.* [7, 9]. The radius measurement reported in Miller *et al.* [8, 10] provides a tighter constraint than that in Riley *et al.* [7, 9], as the former rules out more EOSs on the soft side (c.f. Table II). This difference can be largely traced back to the assumptions underlying the two groups’ analyses. For example, Miller *et al.* used a broader prior on the radius and employed a surface emission model with three hot spots, whereas Riley *et al.* chose a model with two hot spots. In our study as well, we see in Fig. 2 and Fig. 3 that the difference between the two calculations shows up in the mass-radius constraints with radius estimates differing by $\lesssim 0.4$ km on the soft side.

Table II shows the 95% CIs of the radius of a $1.4M_\odot$ neutron star for the models $\text{FRZ}_{2.0}^\chi$ and $\text{FRZ}_{1.5}^\chi$. These results are consistent with existing constraints in the literature. Comparisons of multimessenger posteriors on $R_{1.4M_\odot}$ and $\Lambda_{1.4M_\odot}$ are shown in Fig. 4 and Fig. 5 respectively. There, we see that the 90% CIs are within 10% despite differences in the modeling of neutron-star EOSs and the sets of astrophysical data considered.

Among the various approaches to incorporate low-density nuclear physics inputs, a majority of the works (e.g. [32, 72]) assumed a quadratic expansion in isospin asymmetry that is constrained by the symmetry energy S and its slope L . The recent neutron skin measurement PREX-II favors large S and L , resulting in stiffer nuclear EOS in [32] compared to ours.

Choices for the high-density phase are abundant and range from the piecewise polytrope employed in [30], to the Gaussian-Process-based parameterization in [29]. As expected, this leads to large variations in the posterior. Nevertheless, as the comparisons show, the resulting CIs on $R_{1.4M_\odot}$ and $\Lambda_{1.4M_\odot}$ converge at the level of $\sim 10\%$.

The analyses cited above also considered different sets of astrophysical observations. Raaijmakers *et al.* [30] employed calculations from Miller *et al.* whereas Huth *et al.* [20] combined the constraints from Riley *et al.* as well. As noted earlier, this only has a minor impact (as can be seen from Figure 4). Additional neutron-star radii measurements from quiescent low-mass X-ray binaries (QLMXB) [73] and photospheric radius expansion of X-ray bursting sources (PRE) [74] was incorporated in Steiner *et al.* [75]. These measurements may suffer from unknown systematics, and were not included in our analysis: they appear to only have minor impacts. Lastly, the putative upper limit on neutron-star maximum mass is imposed. Our analysis does not make use of this putative information, resulting in posterior CIs on maximum mass considerably higher than those reported in the literature. Despite this, the posteriors on $R_{1.4M_\odot}$ and $\Lambda_{1.4M_\odot}$ largely agree. This suggests that the properties of canonical $1.4 M_\odot$ neutron stars largely decouple from those of the maximum mass stars even with a simple piecewise polytropic inner core EOS. Indeed, the tighter bounds on M_{max} reported in the literature appear to stem from direct constraints on M_{max} itself via hypotheses based on the post-merger evolution of GW170817 [76, 77].

In this work, we propose a unified parameterization for both chiral EFT-based and phenomenological potential-based pure neutron matter EOSs that allows for natural interpolations between the two nuclear models. This framework enables model selection between the nuclear models, but the current data does not yet provide significant discrimination. For the interpolated model FRZ^ζ , the posterior on ζ marginally shifts towards the EFT-based description, indicating a slight preference for it. This can be largely traced back to the stiffer prior the EFT model admits compared to that of the phenomenological potential-based model (see Fig. 8). We also calculated the log-evidence for FRZ^χ , FRZ^ϕ and FRZ^ζ , which are listed in Table III. As mentioned above, the Bayes factor Eq. (6) can facilitate model selection if it deviates noticeably from unity, by at least a factor of ~ 3 (or $1/3$). The log-evidence listed in Table III do not reveal a significant preference for any of the models suggesting a limited discerning power by current astrophysical observations. We defer to future work on the required error budget for model selection.

Acknowledgments

We thank S. Gandolfi for providing an extended set of QMC phenomenological potential-based EOSs. We also thank Tim Dietrich for carefully reading the manuscript and sharing useful comments. We gratefully acknowledge the use of the high-performance super-computing clusters Kamiak and Pegasus at Washington State University (WSU) and The Inter-University Centre for Astronomy and Astrophysics (IUCAA), respec-

Table III. Global log-evidence (to the base e) from importance sampling [81] for 6 EOS models as one progressively includes more astrophysical observations. The numbers in the brackets are sampling errors written in the scientific notation. The Bayes factors (obtained by taking the exponential of the difference between any two log evidences) for any given observation (row) are not significantly different and do not reveal a preference for any EOS model.

Source	FRZ $_{n_c}^{\chi}$		FRZ $_{n_c}^{\zeta}$		FRZ $_{n_c}^{\phi}$	
	$n_c=1.5$	$n_c=2.0$	$n_c=1.5$	$n_c=2.0$	$n_c=1.5$	$n_c=2.0$
2.08 M_{\odot} Pulsar +GW170817 Miller <i>et al.</i>	-2.34(6) -9.07(6)	-2.35(6) -8.69(18)	-2.67(7) -9.00(8)	-2.67(8) -9.07(8)	-2.41(6) -8.91(4)	-2.48(4) -8.77(6)
PG + 1.44 M_{\odot} Pulsar + 2.09 M_{\odot} Pulsar Riley <i>et al.</i>	-10.73(6) -12.12(20)	-10.57(7) -12.44(8)	-10.91(5) -12.61(8)	-10.87(8) -12.62(6)	-10.83(4) -12.00(5)	-10.69(8) -12.39(12)
PG + 1.32 M_{\odot} Pulsar + 2.07 M_{\odot} Pulsar	-10.30(15) -11.93(7)	-10.40(5) -11.68(20)	-10.75(6) -11.82(15)	-10.61(7) -11.80(20)	-10.45(9) -11.67(14)	-10.24(8) -11.84(7)

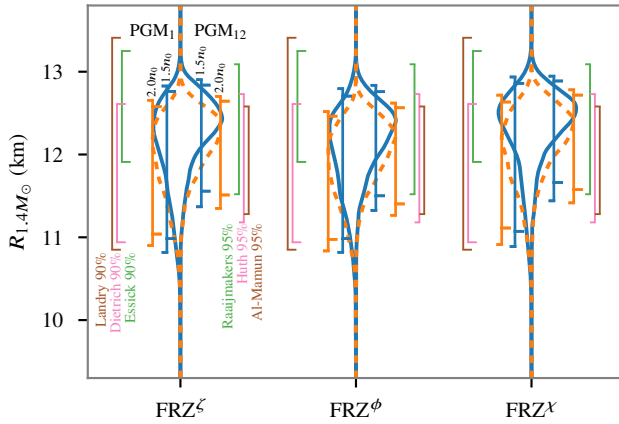


Figure 4. A pair of violins is plotted above for each of the FRZ $^{\zeta}$, FRZ $^{\phi}$, and FRZ $^{\chi}$ models. Each pair consists of two violins – the blue (solid) one is for the transition density of $1.5 n_0$ and the orange (dashed) one is for the transition density of $2 n_0$. The left contour of each violin plots the constraint on the radius of a $1.4 M_{\odot}$ neutron star using three astrophysical observations, namely $2.08 M_{\odot}$ pulsar (P), GW170817 (G), NICER measurements by Miller *et al.* [8] (M_1). On the other hand, the right contour plots the radius constraint after including the second NICER measurement Miller *et al.* [10] (M_2). Double-sided brackets are overlaid for each contour and denote 90% (right facing) and 95% (left facing) CIs. Also drawn are the single sided brackets denoting the 95% CIs for $R_{1.4M_{\odot}}$ in Al-Mamun *et al.* [78], Huth *et al.* [20], Raaijmakers *et al.* [79] and 90% CI obtained by Essick *et al.* [80], Dietrich *et al.* [21], Landry *et al.* [29].

tively. B.B. acknowledges the support from University Grants Commission (UGC), India, the Knut, and Alice Wallenberg Foundation under grant Dnr. KAW 2019.0112, and the Deutsche Forschungsgemeinschaft (DFG, German Research Foundation) under Germany’s Excellence Strategy – EXC 2121 “Quantum Universe” – 390833306. This material is based upon work supported by National Science Foundation (NSF)’s LIGO Laboratory, which is a major facility fully funded by the NSF. P.T., M.M.F. and S.B. acknowledge support from the NSF under Grants PHY-2012190 and PHY-2309352.

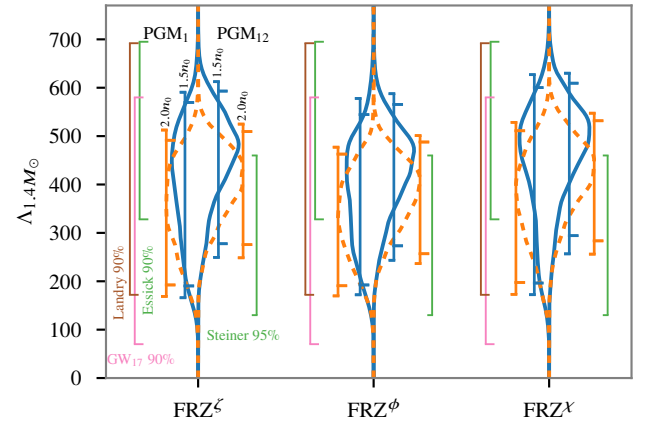


Figure 5. Same as Figure 4 but for tidal deformability of $1.4 M_{\odot}$ stars. Also shown are the for 90% CIs for $\Lambda_{1.4M_{\odot}}$ from GW170817 alone [59]. Additionally, 90% CIs from Essick *et al.* [80], Landry *et al.* [29] and 95% CI by Steiner *et al.* [75] are also drawn.

Appendices

1. Basis from χ EFT Data

Drischler *et al.* [15] used the Gaussian process to fit the data from many-body perturbation theory calculations of χ EFT [82] at various orders of expansion in the ratio of momentum and breakdown scale. Their fitting was performed to account for the truncation errors at increasing orders of expansion. In this work, a breakdown scale of 600 MeV and a momentum cutoff of 500 MeV were chosen to obtain the correlated energy values at selected density points (see Fig. 7). Now, since the energy is parameterized as

$$E_N = m_n c^2 + \kappa \bar{k}^2 + \bar{k}^3 \mathfrak{E}(\bar{k}), \quad (10)$$

and our aim is to model \mathfrak{E} , we calculate the covariance matrix, Σ , for \mathfrak{E} from correlated energy values.

We found that the largest two eigenvalues of Σ – termed d_1 and d_2 – are much larger than the remaining ones. Qualitatively, this means that the variations in \mathfrak{E} are significantly stronger

Table IV. Coefficients of the polynomials fitted to χ_{EFT} data [15] and phenomenological data [36] along with the polynomial fit to the two most dominant eigenvectors of the covariance matrix of the residual energy (as described in Appendix 2).

Polynomial	Coefficients				
	c_4	c_3	c_2	c_1	c_0
\mathfrak{E}_0^ϕ	-172.33	660.87	-905.05	547.612	-140.25
\mathfrak{E}_0^χ	7.8261	-22.787	44.778	-30.786	-7.5286
\mathfrak{E}_1^χ	-2.1849	14.750	-22.012	13.253	-2.8860
\mathfrak{E}_2^χ	11.356	-30.849	30.301	-13.428	2.2623

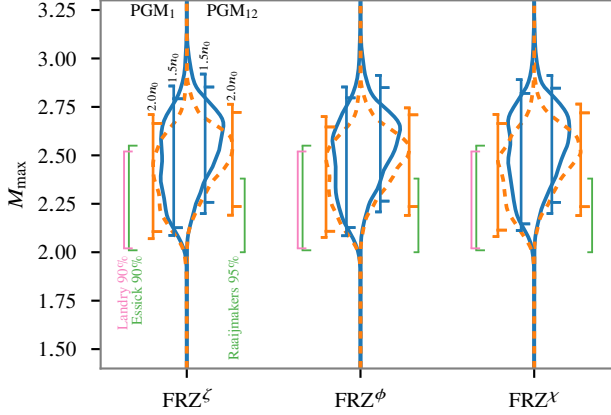


Figure 6. Same as Figure 4 but for M_{max} of neutron stars. Also shown are the 90% CI for M_{max} by Essick *et al.* [80], Landry *et al.* [29] and 95% CI by Steiner *et al.* [75].

along their corresponding eigenvectors than the rest. This observation enables us to represent the variation in \mathfrak{E} as

$$\delta\mathfrak{E} = a_1\sqrt{d_1}V_1 + a_2\sqrt{d_2}V_2. \quad (11)$$

Here, V_i are the two dominant eigenvectors of Σ , and a_i are distributed as $\mathcal{N}(0, 1)$. Therefore, \mathfrak{E} modeled through χ_{EFT} data is given by

$$\mathfrak{E}^\chi = \mathfrak{E}_0^\chi + \delta\mathfrak{E}, \quad (12)$$

where \mathfrak{E}_0^χ is obtained by transforming the mean energy of χ_{EFT} data. We fit $\sqrt{d_{1,2}}V_{1,2}$ and \mathfrak{E}_0^χ with polynomials in \bar{k} . The order of these polynomials (namely, \mathfrak{E}_1^χ , \mathfrak{E}_2^χ and \mathfrak{E}_0^χ) is found to be 4, which is the minimum order that satisfies our requirement that the maximum variance in the error for fitting to the mean energy and eigenvectors is less than 10^{-4} .

2. Basis from Phenomenological Potential Based Data

The phenomenological energy data is discrete and therefore the double derivatives cannot be calculated precisely. This makes the corresponding speed of sound arbitrary. The densities at which energy is provided also vary as we go from one potential to the other. Therefore, we create bins of densities

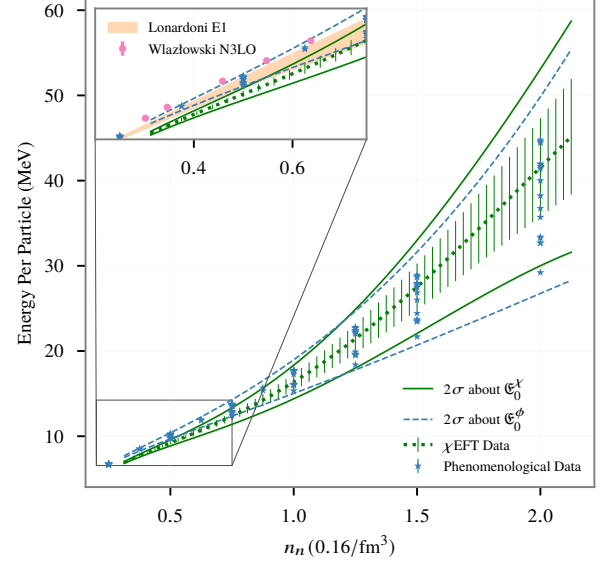


Figure 7. Comparing the χ_{EFT} data [15] (green dotted line with vertical error bars) and phenomenological data [52] (blue stars) with the fits obtained from polynomial models for pure neutron matter. Solid green (dashed blue) line shows the 2σ energy bounds about mean energy of χ_{EFT} data (phenomenological data). Inset plot points out the inconsistencies among different calculations in the energy values of pure neutron matter in the low-density region.

corresponding to the union of density points at which the energies are given. Then, we fit a fourth-order polynomial to individual \mathfrak{E} data to find the missing \mathfrak{E} in these bins. Finally, we find the mean of \mathfrak{E} in all these bins and fit a fourth-order polynomial, in \bar{k} , to this mean energy (call it \mathfrak{E}_0^ϕ).

We find that the variations in the phenomenological \mathfrak{E} can be captured using the eigenvectors of the covariance matrix Σ . That gives the representation of \mathfrak{E} for phenomenological data as

$$\mathfrak{E}^\phi = \mathfrak{E}_0^\phi + \sum_{k=1}^2 c_k \mathfrak{E}_k^\chi. \quad (13)$$

Here, c_1 and c_2 are of order 1. We provide the coefficients of the polynomial fits to the four \mathfrak{E} in Table IV.

The models for the phenomenological and χ_{EFT} data can be

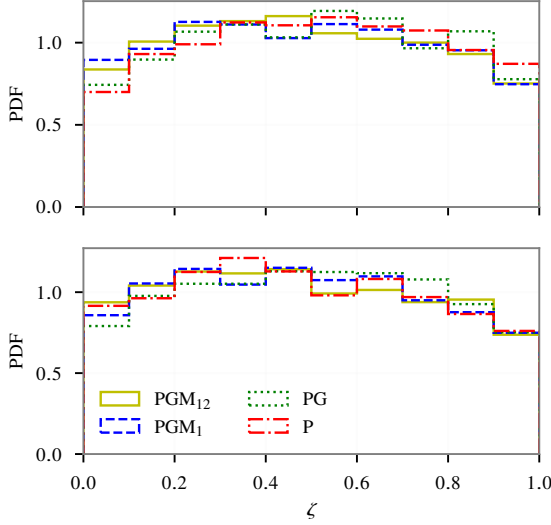


Figure 8. Comparing the ζ distribution after successively adding astrophysical observations for the FRZ_ζ models for transition to core at $1.5n_0$ (top) and $2n_0$ (bottom). The posteriors are dominated by prior and that is why it is flat. This is consistent with the fact that the Bayes' factor between $\text{FRZ}_{1.5}^\chi$ (i.e. $\zeta=0$) and $\text{FRZ}_{1.5}^\phi$ (i.e. $\zeta=1$) is ~ 1 i.e both the extreme points are equally favored. The decrease in the probability at the extreme values are edge effect that can be treated by reweighing the posterior samples with prior samples.

bridged through a translation parameter, ζ . More precisely,

$$\mathfrak{E} = \sum_{k=1}^2 a_k \mathfrak{E}_k^\chi + \mathfrak{E}_0^\chi + \zeta(\mathfrak{E}_0^\phi - \mathfrak{E}_0^\chi). \quad (14)$$

So, our model has three parameters, a_1, a_2 , and ζ . Note that $\zeta = 0$ gives $\mathfrak{E}(\bar{k}) = \mathfrak{E}^\chi$. Using $\mathfrak{E}(\bar{k})$ leads to employing an additional parameter during our Bayesian inference.

One of the main advantages of the model presented here, which is absent in other models based on simulation data, is that it conserves the speed of sound information from the data. And the procedure is general enough to apply to any data in the future. This also provides a natural way of comparing data among different simulations, in light of various microscopic or macroscopic observations.

3. Bayesian Information Criteria

As discussed in the conclusion, the available data does not have enough power to discriminate between the different nuclear models. To see this, we plot the posterior distribution for ζ in Fig. 8 and find that it remains flat.

Although not really needed here, to formally compare the models – including “Occam’s penalty” that should be imposed on FRZ_ζ for using an additional parameter – we compute the Bayesian information criterion (BIC) [84], given by,

$$\text{BIC} = n_{\text{par}} \ln(n_{\text{sam}}) - 2 \ln(\hat{L}), \quad (15)$$

where n_{par} denotes the number of model parameters over which inference is being performed, n_{sam} is the number of posterior samples, and \hat{L} is the maximum likelihood value computed through model parameters. The first term signifies Occam’s penalty whereas the second term quantifies how well the model fits the data. A higher BIC value means the model is less preferred.

Table V gives the BIC values for $\text{FRZ}_{1.5}$ models using likelihoods defined in section III. It shows that the data has no significant preference for either of the two nuclear models, $\text{FRZ}_{1.5}^\chi$ and $\text{FRZ}_{1.5}^\phi$, while the BIC value for the $\text{FRZ}_{1.5}^\zeta$ model is consistently given by $\ln n_{\text{samp}} \approx 10$ – demonstrating Occam’s penalty.

Table V. Bayesian information criterion (BIC) [84] from sampling for 3 EOS models. In each column, various combinations of astrophysical observations are considered in the different rows. A higher value indicates a lesser preference for the model. We see that $\text{FRZ}_{1.5}^\zeta$ gets consistently penalized for having an extra parameter.

Source	$\text{FRZ}_{1.5}^\chi$	$\text{FRZ}_{1.5}^\zeta$	$\text{FRZ}_{1.5}^\phi$
2.08 M_\odot Pulsar	75.83	84.06	75.88
+GW170817	97.57	105.69	96.97
Miller et al.			
PG + 1.44 M_\odot Pulsar	107.00	115.25	106.88
+ 2.09 M_\odot Pulsar	126.37	135.46	126.28
Riley et al.			
PG + 1.32 M_\odot Pulsar	116.46	125.53	116.16
+ 2.07 M_\odot Pulsar	125.85	135.14	125.78

4. Global Sensitivity Analysis

To obtain a Bayesian inference on the EOS models considered in this paper, one must sample a 16- or 17-dimensional parameter space. As more detections are included, this becomes computationally prohibitive, so we perform a global sensitivity analysis to determine the parameters that are most sensitive to the observables. We calculate total effect index $S_T \in [0, 1]$ [57] of each parameter X_i , taking into account its prior:

$$S_T = \frac{E_{X_{-i}}(V_{X_i}(Y|X_{-i}))}{V(Y)}. \quad (16)$$

$$S_T = 1 - \frac{V_{X_{-i}}(E_{X_i}(Y|X_{-i}))}{V(Y)}. \quad (17)$$

Here $E_f(\cdot)$ and $V_f(\cdot)$ are respectively the expectation and variance taken over the “factor” f , which is either the parameter for which the coefficient is being calculated (X_i), or all the parameters *except* the current parameter (X_{-i}).

A large S_T (close to 1) means that the parameter is more sensitive to the specified observable. Based on this measure, we choose highly sensitive parameters for sampling in our inference and fix the less sensitive parameters to a central value described in [33]. We find that the inner core parameters (polytropic indices and transition densities), outer core parameters (a_1 and

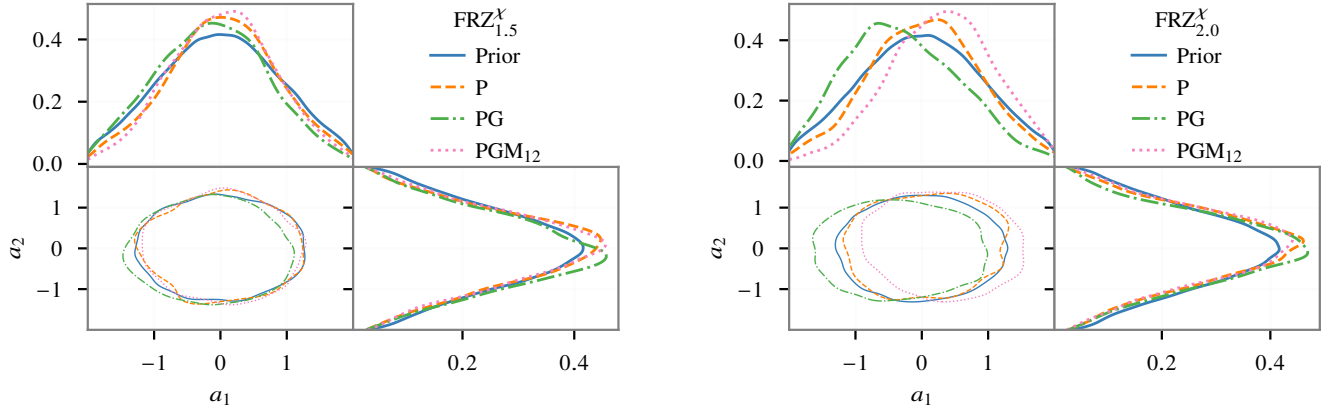


Figure 9. The posteriors of pure-neutron-matter parameters when progressively including the pulsar (P) [83] followed by GW170817 (PG) [1], and finally the multiple NICER (PGM₁₂) [8, 10] observations for the FRZ_{1.5}^X and FRZ_{2.0}^X models.

a_2), and u_p have a total effect index (w.r.t maximum mass,

radius, and tidal deformability) that is at least 2 orders of magnitude higher than the remaining parameters.

-
- [1] B. P. Abbott *et al.* (LIGO Scientific, Virgo), GW170817: Observation of Gravitational Waves from a Binary Neutron Star Inspiral, *Phys. Rev. Lett.* **119**, 161101 (2017), [arXiv:1710.05832 \[gr-qc\]](#).
- [2] B. Abbott, R. Abbott, T. Abbott, F. Acernese, K. Ackley, C. Adams, T. Adams, P. Addesso, R. Adhikari, V. Adya, *et al.*, Properties of the binary neutron star merger gw170817, *Phys. Rev. X* **9**, 011001 (2019).
- [3] J. Aasi *et al.* (LIGO Scientific), Advanced LIGO, *Class. Quant. Grav.* **32**, 074001 (2015), [arXiv:1411.4547 \[gr-qc\]](#).
- [4] F. Acernese *et al.* (VIRGO), Advanced Virgo: a second-generation interferometric gravitational wave detector, *Class. Quant. Grav.* **32**, 024001 (2015), [arXiv:1408.3978 \[gr-qc\]](#).
- [5] B. P. A. *et al.*, Multi-messenger observations of a binary neutron star merger*, *Astrophys. J. Lett.* **848**, L12 (2017).
- [6] B. P. Abbott, R. Abbott, T. D. Abbott, S. Abraham, F. Acernese, K. Ackley, C. Adams, V. B. Adya, C. Affeldt, M. Agathos, *et al.*, Model comparison from LIGO–virgo data on GW170817’s binary components and consequences for the merger remnant, *Class. Quant. Grav.* **37**, 045006 (2020).
- [7] T. E. Riley *et al.*, A NICER View of PSR J0030+0451: Millisecond Pulsar Parameter Estimation, *Astrophys. J. Lett.* **887**, L21 (2019), [arXiv:1912.05702 \[astro-ph.HE\]](#).
- [8] M. C. Miller, F. K. Lamb, A. J. Dittmann, S. Bogdanov, Z. Arzoumanian, K. C. Gendreau, S. Guillot, A. K. Harding, W. C. G. Ho, J. M. Lattimer, R. M. Ludlam, S. Mahmoodifar, S. M. Morsink, P. S. Ray, T. E. Strohmayer, K. S. Wood, T. Enoto, R. Foster, T. Okajima, G. Prigozhin, and Y. Soong, PSR J0030+0451 Mass and Radius from NICER Data and Implications for the Properties of Neutron Star Matter, *Astrophys. J. Lett.* **887**, L24 (2019), [arXiv:1912.05705 \[astro-ph.HE\]](#).
- [9] T. E. Riley, A. L. Watts, P. S. Ray, S. Bogdanov, S. Guillot, S. M. Morsink, A. V. Bilous, Z. Arzoumanian, D. Choudhury, J. S. Deneva, *et al.*, A NICER view of the massive pulsar PSR J0740+6620 informed by radio timing and XMM-Newton spectroscopy, *Astrophys. J. Lett.* **918**, L27 (2021).
- [10] M. C. Miller, F. K. Lamb, A. J. Dittmann, S. Bogdanov, Z. Arzoumanian, K. C. Gendreau, S. Guillot, W. C. G. Ho, J. M. Lattimer, M. Loewenstein, S. M. Morsink, P. S. Ray, M. T. Wolff, C. L. Baker, T. Cazeau, S. Manthripragada, C. B. Markwardt, T. Okajima, S. Pollard, I. Cognard, H. T. Cromartie, E. Fonseca, L. Guillemot, M. Kerr, A. Parthasarathy, T. T. Pennucci, S. Ransom, and I. Stairs, The Radius of PSR J0740+6620 from NICER and XMM-Newton Data, *Astrophys. J. Lett.* **918**, L28 (2021), [arXiv:2105.06979 \[astro-ph.HE\]](#).
- [11] R. B. Wiringa, V. G. J. Stoks, and R. Schiavilla, Accurate nucleon-nucleon potential with charge-independence breaking, *Phys. Rev. C* **51**, 38 (1995).
- [12] B. S. Pudliner, V. R. Pandharipande, J. Carlson, and R. B. Wiringa, Quantum monte carlo calculations of $A \leq 6$ nuclei, *Phys. Rev. Lett.* **74**, 4396 (1995).
- [13] A. Maselli, A. Sabatucci, and O. Benhar, Constraining three-nucleon forces with multimessenger data, *Phys. Rev. C* **103**, 065804 (2021).
- [14] A. Sabatucci, O. Benhar, A. Maselli, and C. Pacilio, Sensitivity of neutron star observations to three-nucleon forces, *Phys. Rev. D* **106**, 083010 (2022).
- [15] C. Drischler, J. A. Melendez, R. J. Furnstahl, and D. R. Phillips, Quantifying uncertainties and correlations in the nuclear-matter equation of state, *Phys. Rev. C* **102**, 054315 (2020).
- [16] J. Lattimer, Neutron stars and the nuclear matter equation of state, *Annual Review of Nuclear and Particle Science* **71**, 433 (2021).
- [17] C. Drischler, J. Holt, and C. Wellenhofer, Chiral effective field theory and the high-density nuclear equation of state, *Annual Review of Nuclear and Particle Science* **71**, 403 (2021).
- [18] R. Essick, I. Tews, P. Landry, S. Reddy, and D. E. Holz, Direct astrophysical tests of chiral effective field theory at supranuclear densities, *Phys. Rev. C* **102**, 055803 (2020).
- [19] J. S. Read, C. Markakis, M. Shibata, K. Uryū, J. D. E. Creighton, and J. L. Friedman, Measuring the neutron star equation of state with gravitational wave observations, *Phys. Rev. D* **79**, 124033 (2009).

- (2009).
- [20] S. Huth, P. T. Pang, I. Tews, T. Dietrich, A. Le Fèvre, A. Schwenk, W. Trautmann, K. Agarwal, M. Bulla, M. W. Coughlin, *et al.*, Constraining neutron-star matter with microscopic and macroscopic collisions, *Nature* **606**, 276 (2022).
 - [21] T. Dietrich, M. W. Coughlin, P. T. Pang, M. Bulla, J. Heinzl, L. Issa, I. Tews, and S. Antier, Multimessenger constraints on the neutron-star equation of state and the hubble constant, *Science* **370**, 1450 (2020).
 - [22] P. T. Pang, I. Tews, M. W. Coughlin, M. Bulla, C. Van Den Broeck, and T. Dietrich, Nuclear physics multimessenger astrophysics constraints on the neutron star equation of state: adding NICER’s PSR J0740+ 6620 measurement, *Astrophys. J.* **922**, 14 (2021).
 - [23] P. T. Pang, T. Dietrich, M. W. Coughlin, M. Bulla, I. Tews, M. Almualla, T. Barna, W. Kiendrebeogo, N. Kunert, G. Masingh, *et al.*, NMMA: A nuclear-physics and multi-messenger astrophysics framework to analyze binary neutron star mergers, *arXiv preprint arXiv:2205.08513* (2022).
 - [24] B. Biswas, P. Char, R. Nandi, and S. Bose, Towards mitigation of apparent tension between nuclear physics and astrophysical observations by improved modeling of neutron star matter, *Phys. Rev. D* **103**, 103015 (2021).
 - [25] S. Ghosh, B. K. Pradhan, D. Chatterjee, and J. Schaffner-Bielich, Multi-physics constraints at different densities to probe nuclear symmetry energy in hyperonic neutron stars, *Frontiers in Astronomy and Space Sciences* **9**, 59 (2022).
 - [26] G. Raaijmakers, S. Greif, T. Riley, T. Hinderer, K. Hebeler, A. Schwenk, A. Watts, S. Nisanke, S. Guillot, J. Lattimer, *et al.*, Constraining the dense matter equation of state with joint analysis of NICER and LIGO/Virgo measurements, *Astrophys. J. Lett.* **893**, L21 (2020).
 - [27] K. Chatziioannou, Neutron-star tidal deformability and equation-of-state constraints, *General Relativity and Gravitation* **52**, 109 (2020).
 - [28] B. Biswas, Bayesian model selection of neutron star equations of state using multi-messenger observations, *Astrophys. J.* **926**, 75 (2022).
 - [29] P. Landry, R. Essick, and K. Chatziioannou, Nonparametric constraints on neutron star matter with existing and upcoming gravitational wave and pulsar observations, *Phys. Rev. D* **101**, 123007 (2020).
 - [30] G. Raaijmakers, S. Greif, K. Hebeler, T. Hinderer, a. Nisanke, A. Schwenk, T. Riley, A. Watts, J. Lattimer, and W. Ho, Constraints on the dense matter equation of state and neutron star properties from nicer’s mass–radius estimate of PSR J0740+ 6620 and multimessenger observations, *Astrophys. J. Lett.* **918**, L29 (2021).
 - [31] I. Legred, K. Chatziioannou, R. Essick, S. Han, P. Landry, *et al.*, Impact of the PSR J0740+ 6620 radius constraint on the properties of high-density matter, *Phys. Rev. D* **104**, 063003 (2021).
 - [32] B. Biswas, Impact of PREX-II and combined radio/NICER/XMM-Newton’s mass–radius measurement of PSR J0740+ 6620 on the dense-matter equation of state, *Astrophys. J.* **921**, 63 (2021).
 - [33] M. Forbes, S. Bose, S. Reddy, D. Zhou, A. Mukherjee, and S. De, Constraining the neutron-matter equation of state with gravitational waves, *Phys. Rev. D* **100**, 083010 (2019).
 - [34] S. Gandolfi, A. Y. Illarionov, K. E. Schmidt, F. Pederiva, and S. Fantoni, Quantum monte carlo calculation of the equation of state of neutron matter, *Phys. Rev. C* **79**, 054005 (2009).
 - [35] S. Gandolfi, J. Carlson, and S. C. Pieper, Cold neutrons trapped in external fields, *Phys. Rev. Lett.* **106**, 012501 (2011).
 - [36] S. Gandolfi, J. Carlson, and S. Reddy, Maximum mass and radius of neutron stars, and the nuclear symmetry energy, *Phys. Rev. C* **85**, 032801(R) (2012).
 - [37] M. Thoennessen, Reaching the limits of nuclear stability, *Rept. Prog. Phys.* **67**, 1187 (2004).
 - [38] P. Hansel, A. Y. Potekhin, and D. G. Yakovlev, Neutron stars 1: Equation of state and structure, vol. 326 of, *Astrophysics and Space Science Library* (2007).
 - [39] W. Zwerger, ed., *The BCS–BEC Crossover and the Unitary Fermi Gas*, Lecture Notes in Physics, Vol. 836 (Springer-Verlag, Berlin Heidelberg, 2012).
 - [40] M. E. Caplan and C. J. Horowitz, Astromaterial Science and Nuclear Pasta, *Rev. Mod. Phys.* **89**, 041002 (2017), *arXiv:1606.03646*.
 - [41] D. Page and S. Reddy, Dense Matter in Compact Stars: Theoretical Developments and Observational Constraints, *Annu. Rev. Nucl. Part. Sci.* **56**, 327 (2006), *arXiv:astro-ph/0608360v1*.
 - [42] K. Fukushima and T. Hatsuda, The phase diagram of dense qcd, *Rep. Prog. Phys.* **74**, 014001 (2011), *arXiv:1005.4814*.
 - [43] A. Kurkela, P. Romatschke, and A. Vuorinen, Cold quark matter, *Phys. Rev. D* **81**, 105021 (2010).
 - [44] J. Lattimer, Neutron stars and the nuclear matter equation of state, *Annual Review of Nuclear and Particle Science* **71**, 433 (2021).
 - [45] M. Fortin, C. Providência, A. R. Raduta, F. Gulminelli, J. L. Zdunik, P. Haensel, and M. Bejger, Neutron star radii and crusts: uncertainties and unified equations of state, *Phys. Rev. C* **94**, 035804 (2016).
 - [46] J. L. Zdunik, M. Fortin, and P. Haensel, Neutron star properties and the equation of state for the core, *Astron. Astrophys.* **599**, A119 (2017), *arXiv:1611.01357 [astro-ph.HE]*.
 - [47] G. Baym, C. Pethick, and P. Sutherland, The Ground State of Matter at High Densities: Equation of State and Stellar Models, *Astrophys. J.* **170**, 299 (1971).
 - [48] F. Fattoyev, C. J. Horowitz, and B. Schuetrumpf, Quantum nuclear pasta and nuclear symmetry energy, *Physical Review C* **95**, 055804 (2017).
 - [49] A. Bulgac, M. Forbes, S. Jin, R. N. Perez, and N. Schunck, Minimal nuclear energy density functional, *Phys. Rev. C* **97**, 044313 (2018).
 - [50] G. Włazłowski, J. Holt, S. Moroz, A. Bulgac, and K. J. Roche, Auxiliary-field quantum monte carlo simulations of neutron matter in chiral effective field theory, *Phys. Rev. Lett.* **113**, 182503 (2014).
 - [51] D. Adhikari *et al.* (PREX), Accurate Determination of the Neutron Skin Thickness of ^{208}Pb through Parity-Violation in Electron Scattering, *Phys. Rev. Lett.* **126**, 172502 (2021), *arXiv:2102.10767 [nucl-ex]*.
 - [52] S. Gandolfi, QMC data (2019), unpublished.
 - [53] D. J. MacKay, *Information theory, inference and learning algorithms* (Cambridge university press, 2003).
 - [54] K. Hebeler, J. M. Lattimer, C. J. Pethick, and A. Schwenk, Equation of state and neutron star properties constrained by nuclear physics and observation, *Astrophys. J.* **773**, 11 (2013), *arXiv:1303.4662 [astro-ph.SR]*.
 - [55] J. M. Lattimer, M. Prakash, D. Masak, and A. Yahil, Rapidly rotating pulsars and the equation of state, *Astrophys. J.* **355**, 241 (1990).
 - [56] G. Raaijmakers, T. E. Riley, A. L. Watts, S. Greif, S. Morsink, K. Hebeler, A. Schwenk, T. Hinderer, S. Nisanke, S. Guillot, *et al.*, A NICER view of PSR J0030+ 0451: Implications for the dense matter equation of state, *Astrophys. J. Lett.* **887**, L22 (2019).
 - [57] A. Saltelli, P. Annoni, I. Azzini, F. Campolongo, M. Ratto, and S. Tarantola, Variance based sensitivity analysis of model output.

- Design and estimator for the total sensitivity index, *Comp. Phys. Comm.* **181**, 259 (2010).
- [58] E. Fonseca, H. T. Cromartie, T. T. Pennucci, P. S. Ray, A. Y. Kirichenko, *et al.*, Refined Mass and Geometric Measurements of the High-mass PSR J0740+6620, *Astrophys. J. Lett.* **915**, L12 (2021).
- [59] B. P. Abbott, R. Abbott, T. Abbott, F. Acernese, K. Ackley, C. Adams, T. Adams, P. Addesso, R. X. Adhikari, V. B. Adya, *et al.*, GW170817: Measurements of neutron star radii and equation of state, *Phys. Rev. Lett.* **121**, 161101 (2018).
- [60] R. E. Kass and A. E. Raftery, Bayes factors, *Journal of the American Statistical Association* **90**, 773 (1995).
- [61] K. Yagi and N. Yunes, Binary Love relations, *Class. Quant. Grav.* **33**, 13LT01 (2016).
- [62] A. Maselli, V. Cardoso, V. Ferrari, L. Gualtieri, and P. Pani, Equation-of-state-independent relations in neutron stars, *Phys. Rev. D* **88**, 023007 (2013).
- [63] B. P. Abbott, R. Abbott, T. Abbott, F. Acernese, K. Ackley, C. Adams, T. Adams, P. Addesso, R. X. Adhikari, V. B. Adya, *et al.*, *EoS-Insensitive Posterior Samples GW170817* (2017).
- [64] M. Gardner and D. Altman, Confidence intervals and statistical guidelines, *Statistics in confidence*. London: BMJ Press, 1 (1989).
- [65] M. C. Miller, F. K. Lamb, A. J. Dittmann, S. Bogdanov, Z. Arzoumanian, K. C. Gendreau, S. Guillot, A. K. Harding, W. C. G. Ho, J. M. Lattimer, R. M. Ludlam, S. Mahmoodifar, S. M. Morsink, P. S. Ray, T. E. Strohmayer, K. S. Wood, T. Enoto, R. Foster, T. Okajima, G. Prigozhin, and Y. Soong, NICER PSR J0030+0451 Illinois-Maryland MCMC Samples, [10.5281/zenodo.3473466](https://arxiv.org/abs/10.5281/zenodo.3473466) (2019).
- [66] M. Miller, F. K. Lamb, A. J. Dittmann, S. Bogdanov, Z. Arzoumanian, K. C. Gendreau, S. Guillot, W. C. G. Ho, J. M. Lattimer, S. M. Morsink, P. S. Ray, M. T. Wolff, C. L. Baker, T. Cazeau, S. Manthripragada, C. B. Markwardt, T. Okajima, S. Pollard, I. Cognard, H. T. Cromartie, E. Fonseca, L. Guillemot, M. Kerr, A. Parthasarathy, T. T. Pennucci, S. Ransom, I. Stairs, and M. Loewenstein, NICER PSR J0740+6620 Illinois-Maryland MCMC Samples, [10.5281/zenodo.4670689](https://arxiv.org/abs/10.5281/zenodo.4670689) (2021).
- [67] T. E. Riley, A. L. Watts, S. Bogdanov, P. S. Ray, R. M. Ludlam, S. Guillot, Z. Arzoumanian, C. L. Baker, A. V. Bilous, D. Chakrabarty, K. C. Gendreau, A. K. Harding, W. C. G. Ho, J. M. Lattimer, S. M. Morsink, and T. E. Strohmayer, A NICER View of PSR J0030+0451: Nested Samples for Millisecond Pulsar Parameter Estimation, [10.5281/zenodo.3386449](https://arxiv.org/abs/10.5281/zenodo.3386449) (2019).
- [68] T. E. Riley, A. L. Watts, P. S. Ray, S. Bogdanov, S. Guillot, S. M. Morsink, A. V. Bilous, Z. Arzoumanian, D. Choudhury, J. S. Deneva, K. C. Gendreau, A. K. Harding, W. C. Ho, J. M. Lattimer, M. Loewenstein, R. M. Ludlam, C. B. Markwardt, T. Okajima, C. Prescod-Weinstein, R. A. Remillard, M. T. Wolff, E. Fonseca, H. T. Cromartie, M. Kerr, T. T. Pennucci, A. Parthasarathy, S. Ransom, I. Stairs, L. Guillemot, and I. Cognard, A NICER View of the Massive Pulsar PSR J0740+6620 Informed by Radio Timing and XMM-Newton Spectroscopy: Nested Samples for Millisecond Pulsar Parameter Estimation, [10.5281/zenodo.7096886](https://arxiv.org/abs/10.5281/zenodo.7096886) (2022).
- [69] J. Buchner, A. Georgakakis, K. Nandra, L. Hsu, C. Rangel, M. Brightman, A. Merloni, M. Salvato, J. Donley, and D. Kovetski, X-ray spectral modelling of the AGN obscuring region in the CDFS: Bayesian model selection and catalogue, *Astron. Astrophys.* **564**, A125 (2014), [arXiv:1402.0004 \[astro-ph.HE\]](https://arxiv.org/abs/1402.0004).
- [70] F. Feroz, M. P. Hobson, and M. Bridges, MultiNest: an efficient and robust Bayesian inference tool for cosmology and particle physics, *Monthly Notices of the Royal Astronomical Society* **398**, 1601 (2009).
- [71] D. W. Scott, *Multivariate density estimation: theory, practice, and visualization* (John Wiley & Sons, 2015).
- [72] I. Tews, J. Margueron, and S. Reddy, Confronting gravitational-wave observations with modern nuclear physics constraints, *European Physical Journal A* **55**, 97 (2019), [arXiv:1901.09874 \[nucl-th\]](https://arxiv.org/abs/1901.09874).
- [73] C. O. Heinke, G. B. Rybicki, R. Narayan, and J. E. Grindlay, A hydrogen atmosphere spectral model applied to the neutron star x7 in the globular cluster 47 tucanae, *Astrophys. J.* **644**, 1090 (2006).
- [74] F. Özel, T. Güver, and D. Psaltis, The mass and radius of the neutron star in exo 1745- 248, *Astrophys. J.* **693**, 1775 (2009).
- [75] A. W. Steiner, S. Gandolfi, F. J. Fattoyev, and W. G. Newton, Using neutron star observations to determine crust thicknesses, moments of inertia, and tidal deformabilities, *Phys. Rev. C* **91**, 015804 (2015).
- [76] B. Margalit and B. D. Metzger, Constraining the Maximum Mass of Neutron Stars From Multi-Messenger Observations of GW170817, *Astrophys. J. Lett.* **850**, L19 (2017), [arXiv:1710.05938 \[astro-ph.HE\]](https://arxiv.org/abs/1710.05938).
- [77] L. Rezzolla, E. R. Most, and L. R. Weih, Using gravitational-wave observations and quasi-universal relations to constrain the maximum mass of neutron stars, *The Astrophysical Journal Letters* **852**, L25 (2018).
- [78] M. Al-Mamun, A. W. Steiner, J. Nättilä, J. Lange, R. O’Shaughnessy, I. Tews, S. Gandolfi, C. Heinke, and S. Han, Combining electromagnetic and gravitational-wave constraints on neutron-star masses and radii, *Phys. Rev. Lett.* **126**, 061101 (2021).
- [79] G. Raaijmakers, S. K. Greif, K. Hebeler, T. Hinderer, S. Nisanke, A. Schwenk, T. E. Riley, A. L. Watts, J. M. Lattimer, and W. C. G. Ho, Constraints on the Dense Matter Equation of State and Neutron Star Properties from NICER’s Mass–Radius Estimate of PSR J0740+6620 and Multimessenger Observations, *Astrophys. J. Lett.* **918**, L29 (2021), [arXiv:2105.06981 \[astro-ph.HE\]](https://arxiv.org/abs/2105.06981).
- [80] R. Essick, I. Tews, P. Landry, S. Reddy, and D. E. Holz, Direct Astrophysical Tests of Chiral Effective Field Theory at Supranuclear Densities, *Phys. Rev. C* **102**, 055803 (2020), [arXiv:2004.07744 \[astro-ph.HE\]](https://arxiv.org/abs/2004.07744).
- [81] F. Feroz, M. P. Hobson, E. Cameron, and A. N. Pettitt, Importance Nested Sampling and the MultiNest Algorithm, *Open J. Astrophys.* **2**, 10 (2019), [arXiv:1306.2144 \[astro-ph.IM\]](https://arxiv.org/abs/1306.2144).
- [82] C. Drischler, K. Hebeler, and A. Schwenk, Chiral interactions up to next-to-next-to-next-to-leading order and nuclear saturation, *Phys. Rev. Lett.* **122**, 042501 (2019).
- [83] H. T. Cromartie *et al.*, Relativistic Shapiro delay measurements of an extremely massive millisecond pulsar, *Nature Astron.* **4**, 72 (2019), [arXiv:1904.06759 \[astro-ph.HE\]](https://arxiv.org/abs/1904.06759).
- [84] H. Akaike, Statistical inference and measurement of entropy, in *Scientific Inference, Data Analysis, and Robustness*, edited by G. Box, T. Leonard, and C.-F. Wu (Academic Press, 1983) pp. 165–189.